JGR Solid Earth

RESEARCH ARTICLE
10.1029/2022JB025226

Nonsystematic Rupture Directivity of Geothermal Energy Induced Microseismicity in Helsinki, Finland

J. M. Holmgren[1], G. Kwiatek[2], and M. J. Werner[1]

[1]School of Earth Sciences, University of Bristol, Bristol, UK, [2]Section 4.2: Geomechanics and Scientific Drilling, Helmholtz Centre Potsdam, GFZ German Research Centre for Geosciences, Potsdam, Germany

Key Points:

- Fluid injection-induced earthquakes provide critical empirical constraints on role of pore pressure versus fault stress in rupture mechanics
- We identify rupture complexity and directivity of induced microseismicity in a pore pressure driven reactivated fracture network
- Events rupture predominantly parallel to the well as mode II failures, providing new constraints for models of rupture growth

Supporting Information:

Supporting Information may be found in the online version of this article.

Correspondence to:

J. M. Holmgren,
joanna.holmgren@bristol.ac.uk

Citation:

Holmgren, J. M., Kwiatek, G., & Werner, M. J. (2023). Nonsystematic rupture directivity of geothermal energy induced microseismicity in Helsinki, Finland. *Journal of Geophysical Research: Solid Earth*, *128*, e2022JB025226. https://doi.org/10.1029/2022JB025226

Received 21 JUL 2022
Accepted 30 JAN 2023

Author Contributions:

Formal analysis: J. M. Holmgren, G. Kwiatek
Investigation: J. M. Holmgren
Methodology: J. M. Holmgren, G. Kwiatek, M. J. Werner
Writing – original draft: J. M. Holmgren
Writing – review & editing: G. Kwiatek, M. J. Werner

Abstract The rupture behavior of microseismicity in fluid-injection settings with low fault stresses is generally believed to be controlled by the pore pressure, including a tendency of the larger induced earthquakes to rupture into the perturbed volume toward the injection well, implying a degree of predictability. Here, we examine directivity patterns to identify fault planes and rupture directions of the 21 largest earthquakes (local magnitudes, M_L 1.3–1.9) recorded during the 2018 St1 Deep Heat geothermal project near Helsinki, Finland. We use the Empirical Green's Function technique to retrieve per-seismic-station corner frequencies, earthquake durations, and directivity trends. After combining the directivity trends with focal mechanisms calculated using principle component analysis, we resolve rupture planes and rupture directions of 10 events. In contrast to studies of induced events at other sites, we find that one event rupture toward, two rupture away, and the remaining rupture parallel to the well. Furthermore, we find that the events prefer mode II failures rather than mode III. These observations provide new constraints for mechanical models of rupture growth in pore-pressure dominated settings.

Plain Language Summary The rupture mechanics of small earthquakes can be challenging to study: their low amplitudes and high frequencies are usually hidden behind noise, affected by attenuation and tend to be difficult to detect at the surface. However, the information they carry can shed valuable light on the behavior of earthquakes in fluid-injection settings, such as deep geothermal sites, where it is important for the operator to know where and how the earthquakes are spreading. In this study, we analyze the rupture behavior of induced microseismicity (local magnitudes <2) that occurred during the 2018 stimulation performed by the St1 Deep Heat geothermal project in Helsinki, Finland. We find that these small earthquake ruptures behave similar to larger earthquakes, implying that the simple models used to describe small earthquakes are not sufficient. Additionally, we find that the largest earthquakes (magnitude 1.5–1.9) generally do not rupture toward the injection well, as predicted in a pore pressure-controlled setting, providing new constraints for rupture growth models.

1. Introduction

Observations of the ruptures of fluid-induced microseismicity provide important information about the underlying processes controlling the earthquakes, such as the role of pore pressure and fault stress in determining rupture direction and maximum magnitude (M_{max}) (e.g., Dempsey & Suckale, 2016; Folesky et al., 2016; Galis et al., 2017; Shapiro et al., 2011). These ruptures can be difficult to study: the small amplitudes require sufficient station coverage at close distances together with high-frequency sensors. When these criteria are fulfilled, however, microseismicity exhibits similar rupture behavior to moderate and large earthquakes, including directivity (Domański & Gibowicz, 2008; Domański et al., 2002; Fan & McGuire, 2018; Jost et al., 1998; Li et al., 1995; Seo et al., 2022) and complex heterogeneous ruptures (Folesky et al., 2016; Kwiatek, 2008). Furthermore, source parameters of small earthquakes can be utilized to better understand the generating mechanisms and to gain insight into the fracture network growth. Such information is essential in the analysis of geomechanical models of stress transfer (e.g., Catalli et al., 2016; Kettlety et al., 2019), fluid pathways (e.g., Igonin et al., 2021), and pre-existing fault structures (e.g., Diehl et al., 2017).

Directivity arises when there is a focus of radiated energy from an earthquake in a particular direction due to a predominant rupture direction (e.g., Haskell, 1964). Assuming a simple, unilateral rupture, seismic stations in the forward rupture direction will experience amplification and increased high-frequency energy, whereas the opposite direction experiences lower amplitudes and less high-frequency energy. In addition to its seismic

hazard implications (e.g., Fletcher & Boatwright, 2020; Kwiatek & Ben-Zion, 2020; Spudich & Chiou, 2008), directivity provides useful information about rupture behavior and the governing mechanisms. Numerical models of earthquake rupture in fluid-injection settings have shown that induced events tend to nucleate at the edge of the stimulated volume and propagate back into the pressurized region with lower friction toward the injection well (Dempsey & Suckale, 2016; McClure & Horne, 2011). Specifically, Dempsey and Suckale (2016) found that ruptures tended to propagate back toward the injection point when injection pressures were high and fault stresses low (i.e., under common conditions of EGS stimulations), while ruptures were more likely to propagate away from the well at low injection pressures. Observational studies of propagation with respect to injection wells have tended to agree with these model predictions. Folesky et al. (2016) studied ruptures of geothermally induced microseismicity in Basel, Switzerland, and found that the largest earthquakes ($M_L \geq 1.8$) ruptured back toward the injection well. For smaller events, the rupture directions were random near the well due to the larger stress perturbations causing failure in randomly oriented cracks, while more homogeneously aligned further away agreeing with preexisting structures and the stress field. Kiraly-Proag et al. (2019) found that the largest induced event, moment magnitude (M_w) 3.3, from the St. Gallen geothermal reservoir, Switzerland, also ruptured toward the injection point. Lui and Huang (2019) found clear rupture directivity with respect to nearby wells for three moderate wastewater injection-induced earthquakes in Oklahoma, USA. Supporting the Dempsey and Suckale (2016) model, the earthquake linked to high injection rates ruptured back toward the wells, while the remaining two events were linked to considerably lower injection and ruptured away from the wells.

Here, we examine directivity patterns of the largest microseismic earthquakes (local magnitudes, M_L 1.3–1.9) recorded during the St1 Deep Heat geothermal stimulation project performed in Espoo, near Helsinki, Finland in summer 2018 (e.g., Hillers et al., 2020; Kwiatek et al., 2019). We identify directivity in 12 out of 21 examined events and find that, even though it is a low fault stress and high injection pressure setting, events are rupturing both toward and away from the injection well. Considering these events occurred during later stimulation stages and in the absence of a distinct pore pressure front, one possible explanation is that the pressure gradient no longer controlled the directivity of the largest events to the same extent as during early stimulation. Instead, later events could be expressing the local stress heterogeneities, stress concentrations, and structure of the fracture zone, allowing for different rupture directions.

2. Data

In 2018, the 6.1 km deep OTN-3 geothermal well in Espoo, Finland, was hydraulically stimulated over 49 days (Hillers et al., 2020; Kwiatek et al., 2019). Two geophone arrays were deployed during the operation (see Figure 1). The nearby OTN-2 well contained ten high-frequency geophones optimal for microseismic detection (e.g., Kwiatek et al., 2019), while the shallow borehole network surrounding the site consisted of 12 4.5 Hz geophones with sampling rates of 500 Hz, located at various depths (0.2–1 km), enabled a better directivity analysis. We use this network to examine azimuthal differences observed in the spectral and temporal content of the earthquakes. We use the catalog by Leonhardt, Kwiatek, Martínez-Garzón, Bohnhoff, et al. (2021), Leonhardt, Kwiatek, Martínez-Garzón, and Heikkinen (2021), who refined the original catalog by Kwiatek et al. (2019). Of the 5,456 relocated events, we analyze the 21 largest events (M_L 1.3–1.9) to investigate directivity effects.

3. Directivity Analysis

Directivity effects are identified by examining the source at different azimuths (e.g., Frankel et al., 1986). In the time domain, the observed source duration, that is, the width of the seismic moment rate (known as the apparent source time function, ASTF), is shorter at stations in the forward rupture direction. Alternatively, the corner frequency of the source spectrum, reflecting the observed high-frequency content, is inversely proportional to the source duration and is thus larger in the forward direction. Figure 2a illustrates the expected source duration, τ_i, and corner frequency, f_{ci}, at station i for a unilateral earthquake for a given double-couple focal mechanism using the Haskell (1964) directivity model:

$$\tau_i = \tau\left(1 - \frac{v_r}{c}\cos\theta_i\right) \quad (1)$$

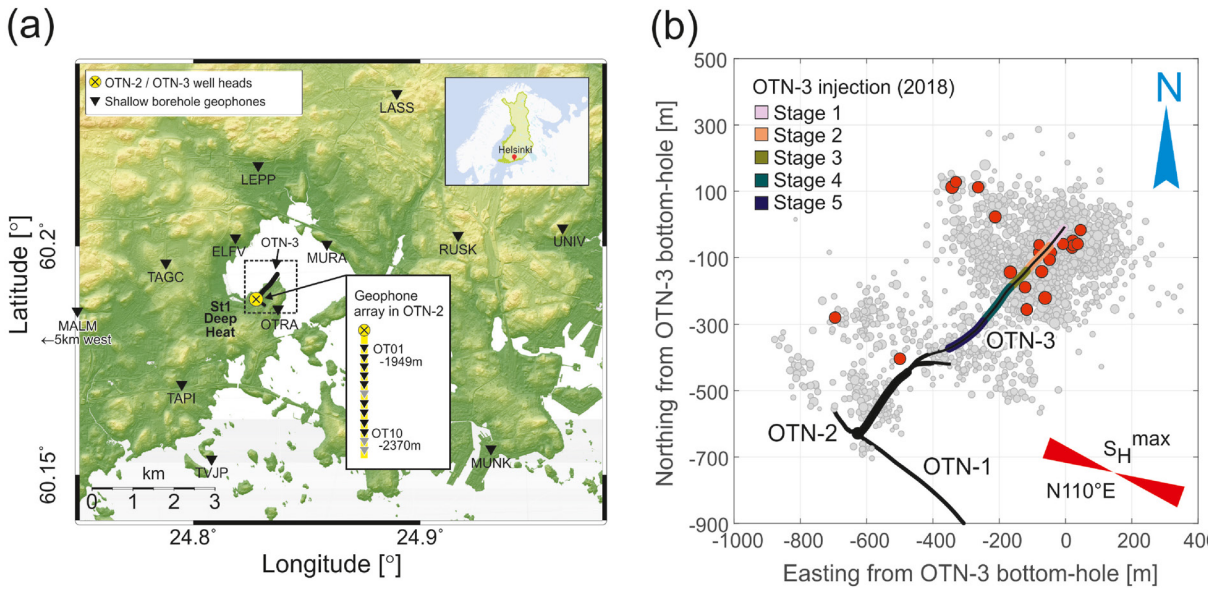

Figure 1. (a) Surface distribution of the seismic sensors monitoring the 2018 stimulation campaign at the St1 Deep Heat project site (yellow circle). (b) Map view of the relocated hypocenters (gray dots) (Leonhardt, Kwiatek, Martínez-Garzón, & Heikkinen, 2021) with magnitude proportional to the size of the circle. Red circles indicate the 21 largest events (M_L 1.3–1.9). The stimulation intervals are shown, color-coded based on stimulation stage (Kwiatek et al., 2019), and maximum horizontal stress ($S_{H\max}$) direction N110°E is indicated (Kakkuri & Chen, 1992).

where τ is the earthquake rupture duration, v_r is the rupture velocity, c is the P- or S-wave velocity, and θ_i is the angle between the rupture and the ray path directions. The term $\cos\theta_i$ can be expanded to cover the full focal sphere (e.g., Park & Ishii, 2015):

$$\cos\theta_i = \sin\gamma\sin\gamma_i + \cos\gamma\cos\gamma_i\cos(\phi - \phi_i) \quad (2)$$

where (γ, ϕ) and (γ_i, ϕ_i) are the dip and azimuth angles of the rupture and take-off directions, respectively. Figure 2a shows that the forward rupture and slip direction, indicated by an arrow, experiences the smallest τ_i and largest f_{ci}. The τ_i then increases symmetrically along the focal sphere away from the rupture direction until it reaches its maximum at the backward direction, and vice versa for f_{ci}. Stations along the auxiliary plane observe constant τ_i and f_{ci}. In more complicated ruptures, such as bilateral ruptures, the resultant τ_i and f_{ci} patterns will be more complex and diverge from symmetry (e.g., Meng et al., 2021). However, any forward rupture directions will still experience smaller τ_i and larger f_{ci} than the rest of the focal sphere.

To analyze directivity effects through τ_i or f_{ci}, we first isolate the earthquake source component through deconvolution using a smaller, co-located Empirical Green's Function (EGF) earthquake (e.g., Abercrombie, Bannister, et al., 2017; Bakun & Bufe, 1975; Holmgren et al., 2019; Mori & Frankell, 1990). Choosing the 21 largest events (M_L 1.3–1.9) as target earthquakes and focusing on the S-wave, we initially select EGF events for each target by examining the 50 closest earthquakes. Using a 0.6 s time window, we cross-correlate the waveforms of the EGF events with the target to ensure similar focal mechanisms and locations. We apply a 15–40 Hz, two-pole, two-pass Butterworth filter to each record, keeping any EGF seismogram with a cross-correlation coefficient (CC) $\geq$0.7 for future steps. Next, we obtain Fourier spectra using multitapering (Prieto et al., 2009) and compute the signal-to-noise ratio (SNR) for each record using a 0.6 s pre-P-phase segment as the noise. We consider frequencies between 7 and 212.5 Hz (85% of the Nyquist frequency). To select target-EGF event pairs, we require SNR $\geq$ 3 starting at maximum 10.5 Hz (1.5 $\times$ minimum considered frequency) and encompassing a minimum bandwidth of 50 Hz. With potential EGF events selected for each target event at each station, we begin our directivity analysis by examining station variations in f_{ci}.

The source spectrum of an earthquake can be described by the omega-squared model (Boatwright, 1980; Brune, 1970):

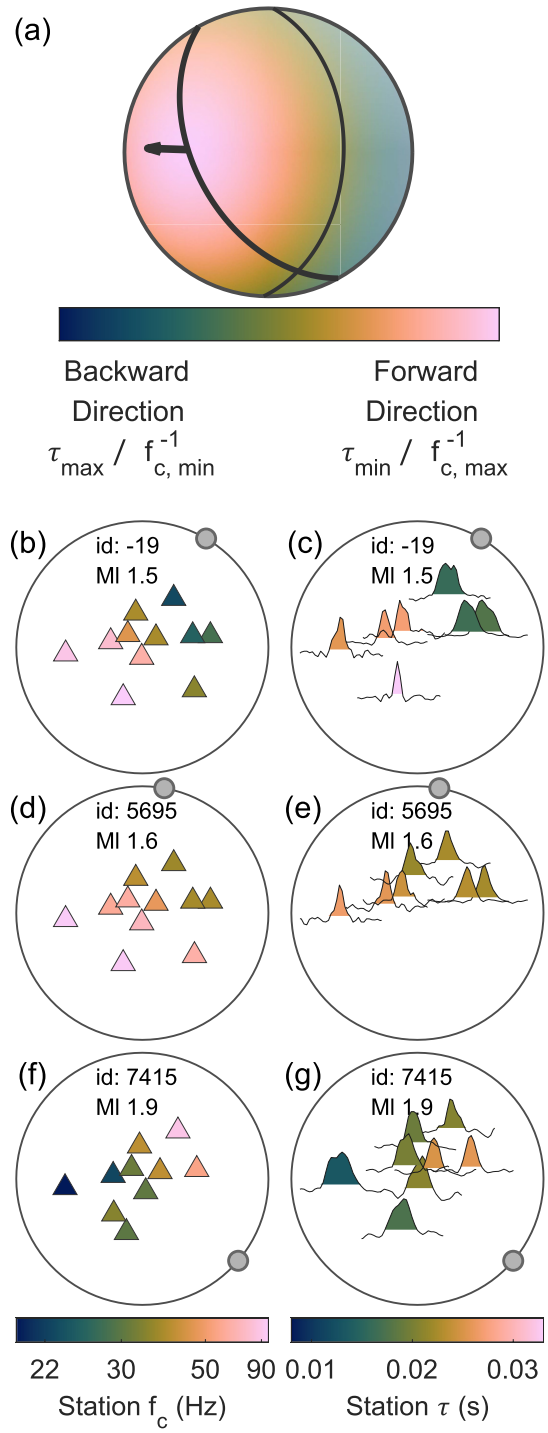

Figure 2. (a) Modeled directivity pattern given an example focal mechanism for a simple, unilateral rupture. The arrow indicates the rupture direction on the fault plane, coinciding with slip direction. (b, d, f) Three example earthquakes showing a change in station f_{ci} on the focal sphere (upper hemisphere, equal-area projection). The triangles indicate the station location on the focal sphere. The gray circle on the edge of the sphere indicates the direction to the closest point on the well. (c, e, g) Same three earthquakes, but showing the stations' ASTFs colored by τ_i.

$$\Omega(f) = \frac{\Omega_0}{\left[1 + \left(\frac{f}{f_c}\right)^{2\gamma}\right]^{\frac{1}{\gamma}}} \tag{3}$$

where Ω_0 is the low-frequency plateau, f is the frequency, f_c is corner frequency, and γ is a constant defining the sharpness of the corner. We use the Boatwright (1980) model with $\gamma = 2$. In the EGF method, the spectral ratio between the target and EGF events is:

$$\frac{\Omega_T(f)}{\Omega_{\mathrm{EGF}}(f)} = \frac{\Omega_{0,T}}{\Omega_{0,\mathrm{EGF}}} \frac{\left[1 + \left(\frac{f}{f_{c,\mathrm{EGF}}}\right)^{2\gamma}\right]^{1/\gamma}}{\left[1 + \left(\frac{f}{f_{c,T}}\right)^{2\gamma}\right]^{1/\gamma}} \tag{4}$$

where subscripts T and EGF indicate target and EGF. For each target-EGF record pair we compute the spectral ratio in the frequency domain. We discard any spectral ratios where the low-frequency ratio ($\Omega_{0,T}/\Omega_{0,\mathrm{EGF}}$) is less than 5.6, equivalent to a M_w difference (ΔM_w) less than 0.5, to ensure the EGF is small enough. For each station with a minimum of four spectral ratios, we stack the normalized spectral ratios and use nonlinear least squares to fit the stack to Equation 4 and solve for $f_{c,T}$ (i.e., f_{ci}). Following Viegas et al. (2010) and Abercrombie, Bannister, et al. (2017), the $f_{c,T}$ uncertainty bounds are defined as the minimum and maximum frequencies over which the variance is within 5% of the minimum variance. We also test a stricter ΔM_w criterion of 1.0 (equivalent to a low-frequency ratio of 31.6), which is commonly used to ensure the delta function assumption holds (e.g., Abercrombie, Bannister, et al., 2017; Huang et al., 2017; Onwuemeka et al., 2018). While this removed 5,471 individual spectral ratios out of 10,240 spectral ratios in total and several station stacks, we find that the final station $f_{c,T}$ results do not change significantly and stay within the $f_{c,T}$ uncertainty bounds from the 0.5 ΔM_w results, thus deciding to keep the 0.5 ΔM_w criterion. Of the 21 analyzed target earthquakes, 12 exhibit clear spatial variations in f_{ci}, spanning M_L between 1.4 and 1.9. Three of these are shown in Figures 2b, 2d and 2f. See Figures S1–S21 in Supporting Information S1 for the analyzed events' waveform timeseries and spectral ratio stacks at each station.

We next investigate directivity effects in the time domain by deconvolving the targets by their EGFs to obtain ASTFs (e.g., Hartzell, 1978). First, to ensure the EGF duration is small enough to satisfy the delta function assumption and avoid underestimating the ASTF pulse width (e.g., Lanza et al., 1999), we use the $f_{c,T}$ and $f_{c,\mathrm{EGF}}$ outputs (Equation 4). Considering τ is inversely proportional to f_c, we generate far-field STF pulses representing targets and EGFs of different magnitude and stress drop ranges and investigate how much smaller the EGF pulse width (τ_{EGF}) is required to be to retrieve the target pulse width (τ_T) from the deconvolved ASTF. We find that $\tau_T/\tau_{\mathrm{EGF}} \geq 2.5$ resolves the ASTF pulse width to within 75% of the true target duration, thus requiring $f_{c,\mathrm{EGF}}/f_{c,T} \geq 2.5$ to compute ASTFs. We also tried using a stricter criterion of $f_{c,\mathrm{EGF}}/f_{c,T} \geq 4.0$ (resolving to within 85% of τ_T) but found that the output ASTFs were close to identical albeit significantly fewer. Next, to ensure the ASTFs are stable, we use a water level correction of 0.001 (e.g., Mueller, 1985). To remove the high-frequency noise, we apply a 212.5 Hz low-pass filter (85% of the Nyquist frequency). Finally, for each target earthquake, we stack all normalized ASTFs for each station. We calculate τ_i values

by estimating the width of the stacked ASTFs at 0.1 of the maximum amplitude (Courboulex et al., 2016). We define the τ_i uncertainty as the sampling rate ($\pm$0.002 s).

Of the 21 target earthquakes, 10 events display τ_i directivity effects. These 10 are included in the 12 events with directivity from the f_{ci} results. The remaining earthquake with clear f_{ci} variation has too few resolvable station ASTFs to determine τ_i directivity. Station ASTFs are shown for three directivity events in Figures 2c, 2e and 2g. Based on visual inspection, eight of the 21 events also displayed complex ruptures: the ASTF shape deviates from a simple pulse (e.g., Figures 2c and 2g). Complexity in the frequency domain is difficult to model and typically appears as bumps altering the spectral shape (e.g., Holmgren et al., 2019; Uchide & Imanishi, 2016), resulting in biased f_{ci} estimates. However, while complexity is easier to identify in the time domain, we find fewer ASTFs in the Helsinki data set and thus the f_{ci} results provide overall better focal sphere coverage. Furthermore, identical trends for f_{ci} and τ_i suggests that f_{ci} is a useful indicator of forward rupture directions even if the rupture is complex.

4. Focal Mechanism Reassessment

Leonhardt, Kwiatek, Martínez-Garzón, Bohnhoff, et al. (2021) determined focal mechanisms for 191 earthquakes from station polarities using a cross-correlation technique and manual inspection. They identified three distinct families with oblique reverse faulting as the dominant source mechanism type, a mechanism not easily resolved with the available station coverage. Due to the combination of deep microseismicity (~6.1 km) and relatively small epicentral distances to stations (≤9 km), the focal sphere station coverage is clustered toward the center of a compressional quadrant. Thus, constraining the locations and orientations of the nodal planes depends on the few stations at the network edges with lower SNR. Leonhardt, Kwiatek, Martínez-Garzón, Bohnhoff, et al. (2021) found that Family 1 was fairly well constrained with consistent polarities, but the remaining two families displayed more polarity variation between events and were less stable.

We refine the focal mechanisms using a Principle Component Analysis (PCA) approach (Vavrycuk et al., 2017), which combines classical amplitude and waveform-based moment tensor (MT) inversion techniques and is suitable for microseismic, high-frequency events with low SNR. First, we apply a 5–20 Hz, two-pole Butterworth filter to each target earthquake displacement record at each station, extracting 2.0 s time windows centered on the P-wave arrival. For each event, we taper the station waveforms, align them using cross-correlation, and extract the common source wavelet (see details in Vavrycuk et al., 2017). Finally, we retrieve MTs through classical MT-amplitude inversion (hybridMT, Kwiatek et al., 2016), using the PCA coefficients as input. We calculate stable double-couple constrained MTs with small non-double couple components for 19 of the 21 events (see Figure 3 and Table S1 in Supporting Information S1). The additional usage of wavelet-based amplitude input leads to more homogeneous oblique reverse focal mechanisms consistent with Family 1 of Leonhardt, Kwiatek, Martínez-Garzón, Bohnhoff, et al. (2021) (see Figure S22 in Supporting Information S1). The changes in focal mechanisms are primarily due to improvement of ambiguous P-wave polarity from stations located close to nodal planes. The obtained mechanisms, regardless of nodal plane, are well oriented within the stress field (cf. Figure 10 in Leonhardt, Kwiatek, Martínez-Garzón, Bohnhoff, et al., 2021). We find that the PCA approach is well-suited for MT inversion of small earthquakes by building on amplitude-based inversion and yet being less complex than a full-waveform approach (see discussion in Bentz et al., 2018). For example, because it relies on the area under the P-wave pulse, it is less sensitive to directivity patterns than the classical amplitude-based inversions. Furthermore, path and site effects are diminished because the sensors are located in boreholes drilled into crystalline Precambrian Svecofennian basement rock with very low attenuation (e.g., Kwiatek et al., 2019), allowing for reliable focal mechanism solutions even though the earthquakes' small magnitudes require source analysis in the higher frequencies (here, we focus on the frequency range 5–20 Hz). Eulenfeld et al. (2022) analyzed attenuation effects using the Helsinki induced events and found that the quality factor is larger than 1000 for frequencies above 10 Hz. Abercrombie (1995) found that using deep borehole sensors removed the severe attenuation that occurs in the upper kilometers in a granite batholith at the Cajon Pass, California. We note that Ide et al. (2003) reported strong path and site effects in a deep borehole at the Long Valley caldera in California, however, the attenuation properties of a volcanic caldera are significantly different to a crystalline batholith.

5. Combining Directivity and Focal Mechanisms

Next, we combine the focal mechanisms and observed directivity to identify fault planes from auxiliary planes and invert for the earthquake rupture directions using Equation 1 (e.g., Jost et al., 1998; Li et al., 1995). Because

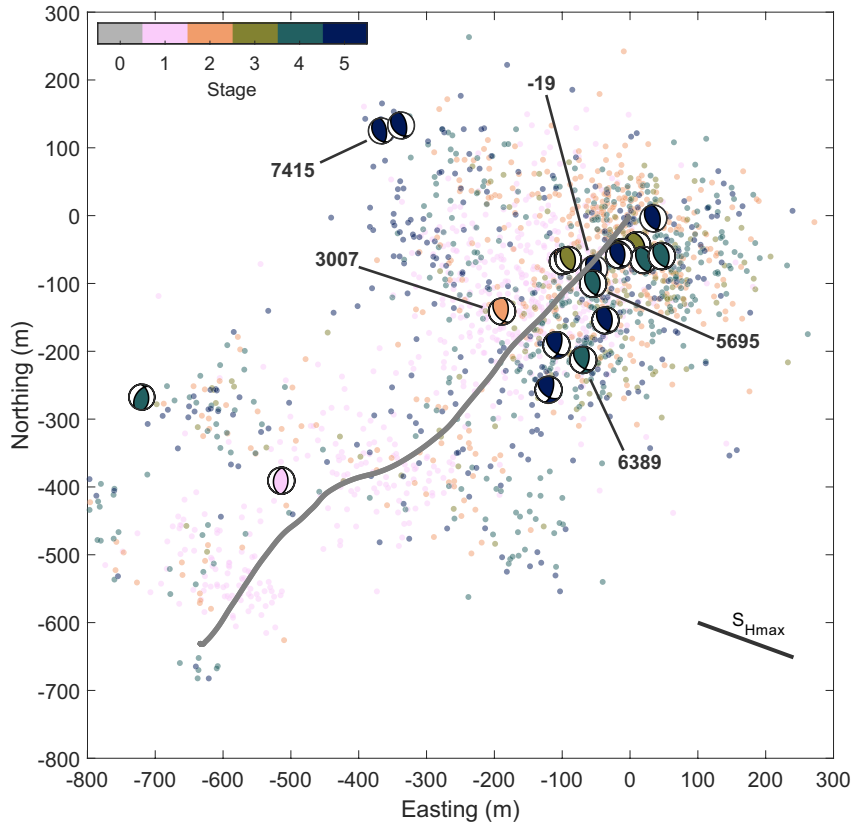

Figure 3. PCA-based focal mechanisms (upper hemisphere projection) for the 19 earthquakes with solutions plotted over the event catalog from Leonhardt, Kwiatek, Martínez-Garzón, and Heikkinen (2021), colored based on injection stage. Numbers denote catalog event ID. Maximum horizontal stress ($S_{H\max}$) direction N110°E is indicated with a line (Kakkuri & Chen, 1992; Kwiatek et al., 2019).

the observed directivity has better station coverage in the frequency domain than in the time domain, we use the observed $f_{\rm ci}$ estimates converted to τ_i instead of the observed τ_i estimates directly. A conversion commonly assumed in the literature is simply $\tau \simeq 1/f_c$ (e.g., Archuleta & Ji, 2016; Van Houtte and Denolle, 2018). Empirically, Prieto et al. (2017) found a similar conversion ($\tau = 0.94/f_c$) for a 75 km deep M_w 4.8 earthquake. Meanwhile, Hisada (2000) theoretically determined $\tau = 1/(2f_c)$, while Denolle and Shearer (2016) assumed $\tau = 1/(\pi f_c)$. Tomic et al. (2009) computed both spectral ratios and ASTFs using the EGF method to investigate stress drops of $M_L \leq 2.1$ induced earthquakes in Brazil. After converting their reported averaged rupture radii back to f_c and finding the mean duration for each event (see Tables 2 and 3, Tomic et al., 2009), their earthquakes also show a $\tau = 1/(x\, f_c)$ relation, where x varies between 1.06 and 1.58 between the events. Here, we empirically investigate the relationship between f_c and τ to find the most suitable conversion. Using all the event-station pair stacks with both measured $f_{\rm ci}$ and τ_i estimates, we determine a linear empirical relationship between the values (see Figure 4a). To ensure the τ_i values are not too small to be resolvable considering the 500 Hz sampling rate, we first synthetically examine the minimum number of samples required inside a pulse to estimate the pulse width (see Figures S34–S38 in Supporting Information S1). For a symmetrical pulse, we find ≥ six samples can resolve the pulse width within 5% of the true width. For the Helsinki data, which has a sampling rate of 500 Hz, a minimum of six samples corresponds to a minimum ASTF pulse width $\tau_i = 0.012$ s. This minimum limit is indicated as a dashed horizontal line in Figure 4a and we find that the τ_i versus $1/f_{\rm ci}$ relationship below this limit does not visually follow the same trend as the remaining data. We find the following relationship between the measured τ_i and $f_{\rm ci}$ estimates:

$$\tau_i = \frac{1}{3.04\, f_{\rm ci}} + 0.011 \tag{5}$$

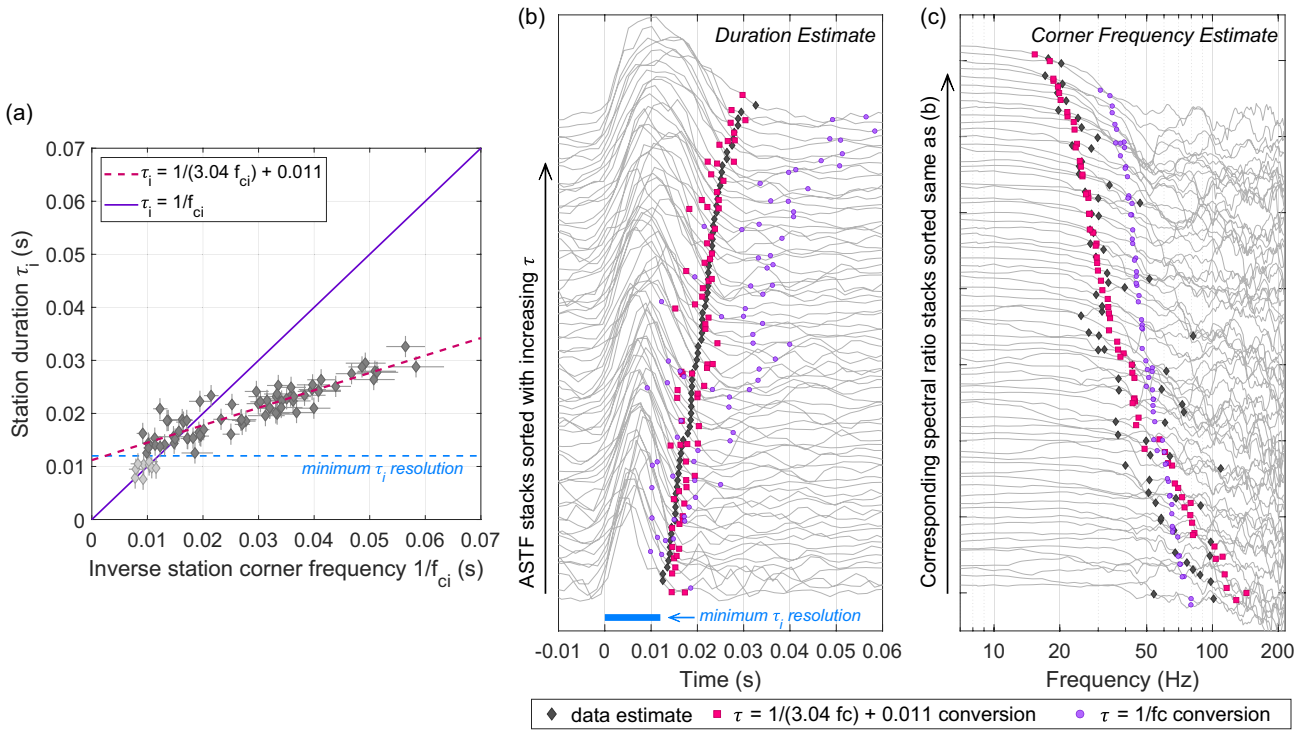

Figure 4. (a) Linear empirical relationship between the observed τ_i and inverse f_{ci} estimates. The solid line shows the $\tau = 1/f_c$ relationship and the dashed line shows the best-fit line between the estimates. The minimum observed τ_i resolution is indicated as a horizontal dashed line, corresponding to $\tau_i = 0.012$ s, and data smaller than this limit are shown as lighter shaded diamonds. The τ_i and f_{ci} uncertainties are indicated as vertical and horizontal bands, respectively. (b) Apparent source time function (ASTF) stacks for all the event-station pairs which also had a spectral ratio stack. The ASTF pulses are aligned to start at time 0.0 s and ordered with increasing observed τ_i (dark diamonds). For each ASTF stack, the τ_i estimated from the corresponding observed spectral ratio f_{ci} using Equation 5 are shown as pink squares, and the τ_i estimates using the $\tau = 1/f_c$ conversion are shown as purple circles. (c) The corresponding spectral ratio stacks to the ASTFs stacks shown in (b). Each stack's observed f_{ci} is shown as a dark diamond, and the f_{ci} conversions using the corresponding observed τ_i measurements are shown with similar colors to (b).

Seeing how close 3.04 is to π, Equation 5 agrees the most with the $\tau = 1/(\pi f_c)$ conversion used in Denolle and Shearer (2016). To visually inspect this relationship further, we also include the event-station ASTF and spectral ratio stacks in Figures 4b and 4c with their τ_i and f_{ci} estimates shown (dark diamonds). Using the corresponding f_{ci} or τ_i measurements, we calculate the resultant τ_i or f_{ci} using Equation 5 (pink squares). We also include the resultant τ_i or f_{ci} estimates using the commonly assumed $\tau \simeq 1/f_c$ relationship (purple circles). As can be seen, the $\tau \simeq 1/f_c$ conversion leads to overestimation in both τ_i and f_{ci} at longer durations and lower corner frequencies, respectively.

For the inversion, we constrain the possible rupture directions to the two nodal planes, assuming unilateral rupture. In short, we find the optimum rupture direction for each nodal plane and then determine the earthquake's optimum rupture direction by comparing the root-mean-square (rms) residuals of the two directions. Figure 5 illustrates the inversion process for the largest event, 6389 (M_L 1.9). We let the strikes and dips obtained from the focal mechanism solutions constrain the possible rupture directions in the inversion and solve for a best-fit rupture angle on the planes for the rupture direction to retrieve θ_i from Equation 1. This is done by combining the rupture angle, strike, and dip to give us a plunge and trend of the rupture direction on the plane. The plunge and trend are then used to calculate the distance along the sphere to each station, that is, θ_i. For each of the two nodal planes, we solve for the rupture angle, v_r, and τ using the nonlinear least-squares inversion in MATLAB, also extracting the Jacobian to retrieve the 68% confidence interval for each parameter as an uncertainty measure. Thus, our objective function becomes:

$$f(\theta_i, v_r, \tau) = \tau\left(1 - \frac{v_r}{c}\cos\theta_i\right) - \tau_i \tag{6}$$

where τ_i values are obtained by converting the observed f_{ci} using Equation 5. After the two nodal planes' optimum rupture directions and their uncertainties have been found, we conduct a grid search around their rupture-angle uncertainty bands to evaluate which rupture direction is the earthquake's most-likely rupture direction (and thus

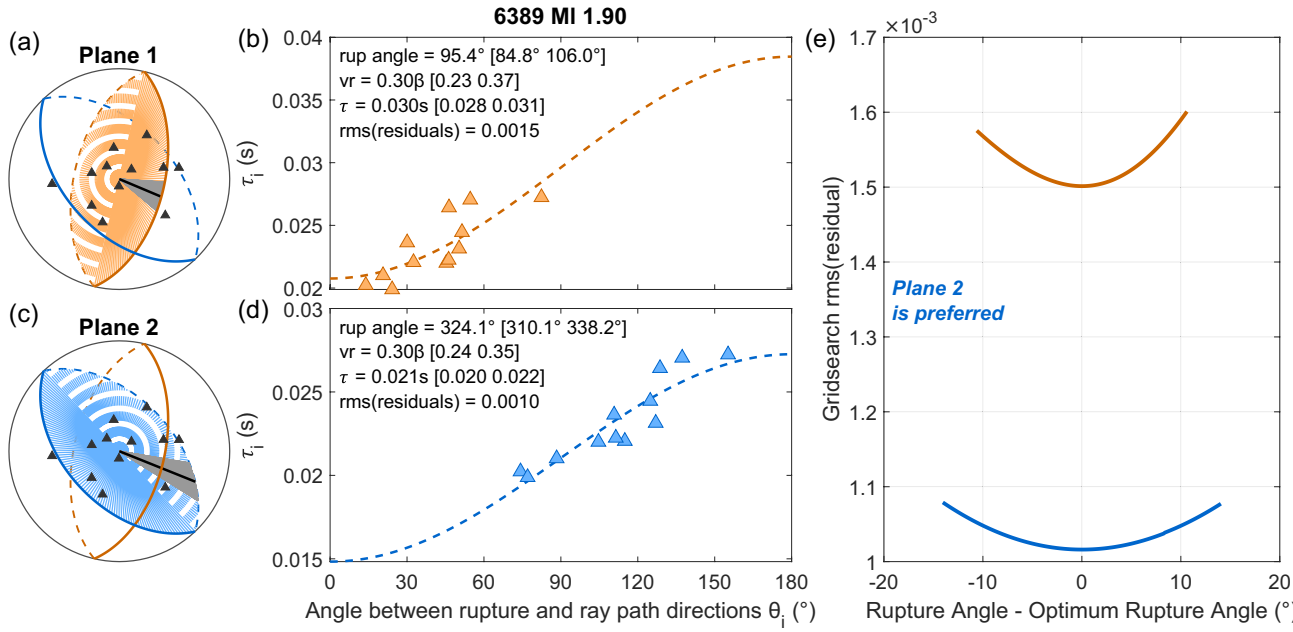

Figure 5. Rupture direction inversion scheme for event 6389 and its two nodal planes. (a) Shows nodal plane 1 on the focal sphere and the possible rupture angle directions. Dashed and solid lines indicate lower and upper hemisphere, respectively. The black solid line shows the best-fit rupture direction on the plane and the gray area indicates the 68% confidence interval of the best-fit direction. Triangles show the locations of the stations used (upper hemisphere). (b) Dashed line shows the model fit for the best-fit rupture direction for plane 1 and triangles indicate the converted τ_i versus θ_i (angle between rupture direction and station ray path from Equation 1). (c, d) Same as (a, b) but for nodal plane 2 for the same event. (e) Grid search around the optimum rupture angle direction's 68% confidence interval plotted against the root-mean-square (rms) residual. For this event, plane 2 has the lowest rms(residual) and is the preferred nodal plane.

which nodal plane is the fault plane). For each evaluated rupture angle in the grid search (see Figure 5e), we let v_r and τ be free parameters and redo the inversion to compute the rms of the residuals. If one of the planes has lower rms(residuals) over its full confidence interval, we select this as the event fault plane and rupture direction. If the rms(residuals) overlap over the confidence intervals, both nodal planes and rupture directions are kept (see Figures S23–S33 in Supporting Information S1 for more event examples).

Out of the 12 events with directivity, we constrain one best-fit rupture direction for 10 events and two possible rupture directions for two events (see Table S2 in Supporting Information S1). The inverted rupture direction(s) for each earthquake is shown in Figures 6a and 6b, where the rupture direction is indicated and colored based on angle with respect to the well. Most of the events appear to rupture parallel to the well. Two events out of the 10 events with one resolvable rupture directions rupture away from the well: events 5695 (M_L 1.6) and 6389 (M_L 1.9, the largest event) both occurring during stimulation stage 4. However, when considering the ambiguity in nodal planes and the 52-m catalog location uncertainty (Leonhardt, Kwiatek, Martínez-Garzón, Bohnhoff, et al., 2021), the rupture direction with respect to the well is more uncertain for event 5695, which occurred close to the well (44 m away). To investigate this further for each event, we let the rupture direction stay the same but let the earthquake location change along a sphere centered at the event hypocenter with a 52-m radius. We compute the rupture angle at each point on the sphere to examine how much it changes considering the location uncertainty (see Figure S39 in Supporting Information S1). Unsurprisingly, we find that the events within 55 m of the well (events 4364, 5695, 5386, and 7641) are much more sensitive to the location uncertainty and their rupture angles are less stable. However, the largest event, event 6389, occurred 132 m away and thus still unequivocally ruptured away from the well, not toward the well as found at other geothermal sites (e.g., Folesky et al., 2016; Kiraly-Proag et al., 2019). We also examine the evolution of the rupture angle with respect to time and distance from the well (see Figure 6c), finding no clear trend.

Finally, we use the rupture angles on the fault planes to investigate the prevalence of mode II (in-plane shearing, slip and rupture are parallel) and mode III (out-of-plane shearing, slip and rupture are perpendicular) failures among the earthquakes. For each event, we find the angle between the rupture angle and the rake angle from the focal mechanism solutions (Figure 7a), where 0° and 180° (i.e., rupture parallel to the slip direction) indicates

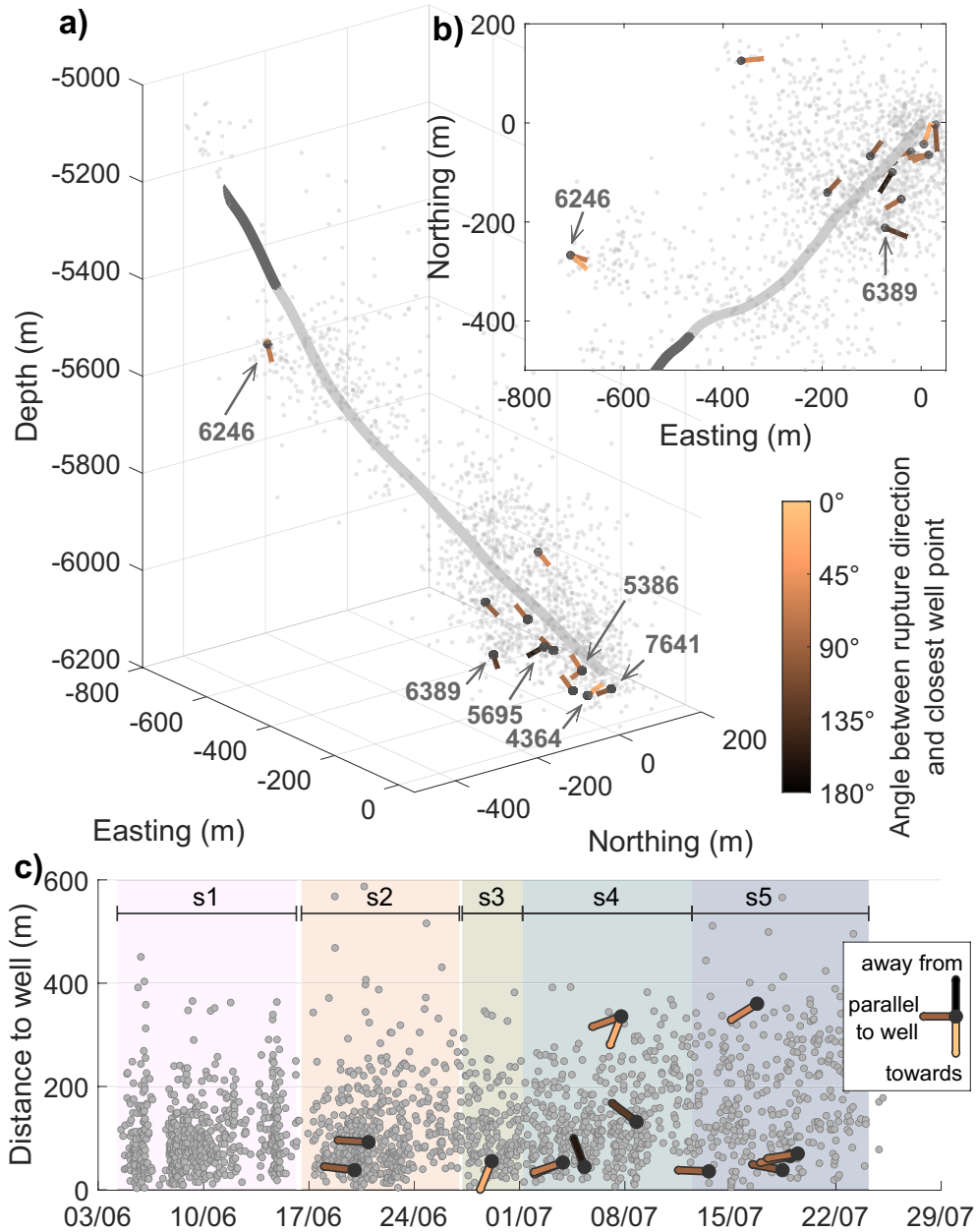

Figure 6. (a) 3D view of the OTN-3 well and surrounding seismicity cloud. The 12 targets with observed directivity are shown as black points. The best-fit rupture directions are indicated by lines extending from each event, showing two lines for events with two possible directions. The line color indicates the angle between the rupture direction and the well, where 0° is toward the well and 180° is away. (b) Same as (a) but in map-view. (c) r-t plot showing the earthquake distance from the closest point on the well plotted against time. The rupture direction is indicated for the 12 directivity events, following the same color scheme as for (a, b). Background is colored by the stimulation stage.

pure mode II and 90° and 270° indicates pure mode III failure. Figure 7b shows a polar histogram of the angles found, indicating a preference toward mode II failures among the 12 directivity earthquakes.

6. Discussion

Knowledge about the fault plane orientations and rupture directions of fluid-induced seismicity offer important insight into the driving forces governing earthquake behavior. Such information is essential to estimating key parameters such as maximum rupture size and M_{max}: rupture growth models have shown that pore-pressure

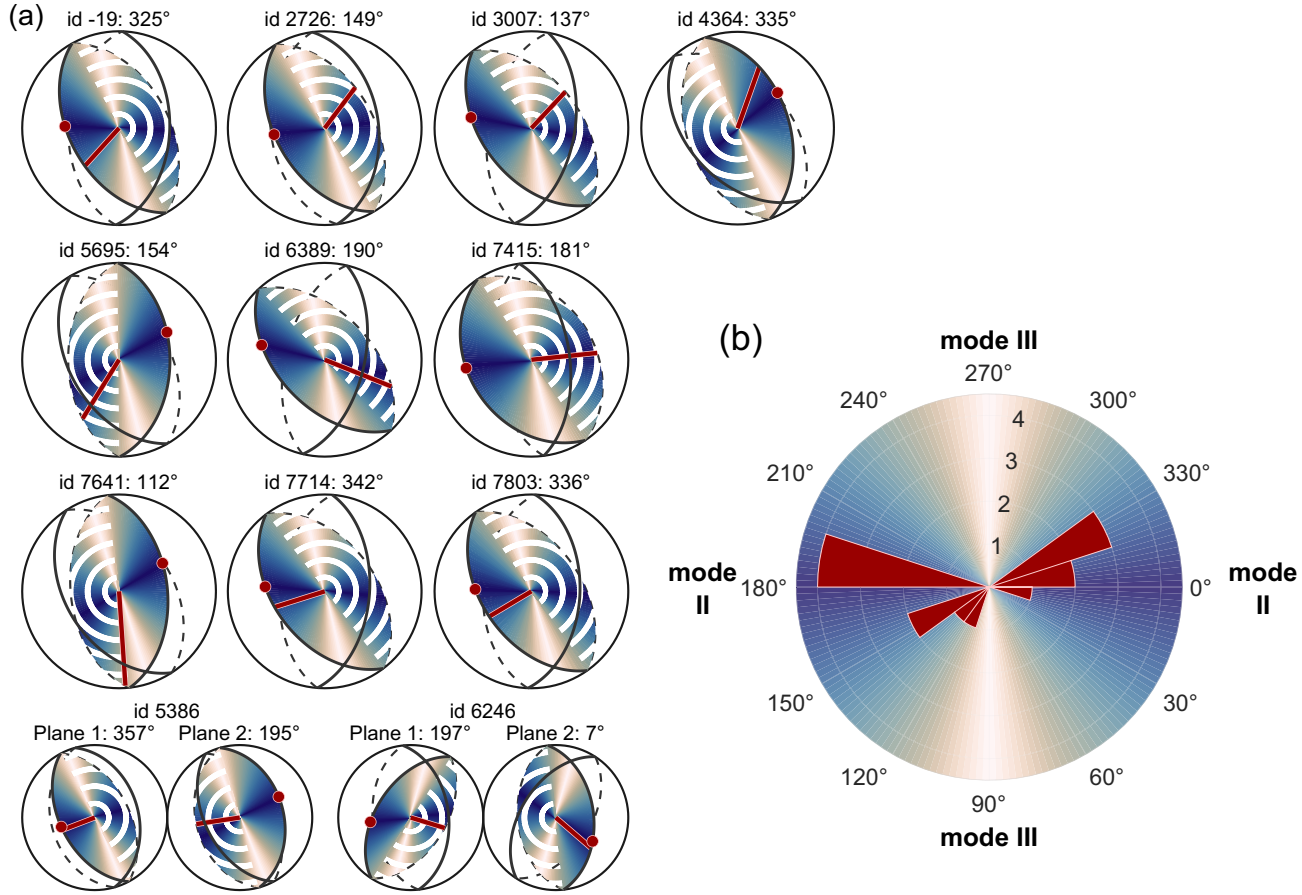

Figure 7. Failure modes compared to rupture directions. (a) Rupture direction on the fault plane for each event displaying directivity. The planes are colored based on angle from the fault plane's rake, reflecting mode II failure at 0° and 180° as darker blue shades and mode III at 90° and 270° as lighter shades. The rake angle is indicated by a red circle and rupture direction by a red line. Upper hemisphere of the focal sphere is shown by solid color on the plane, while lower hemisphere is shown as dashed. Events 5386 and 6246 (bottom row) have two rupture direction solutions each. (b) Rupture directions with respect to the fault plane's rake (calculated clockwise) for all directivity events plotted as a polar plot, where background shading reflects mode II or mode III failures as in (a).

driven seismicity is more likely to be constrained within the perturbed zone (e.g., Dempsey & Suckale, 2016; Galis et al., 2017; Gischig, 2015; McClure & Horne, 2011; Shapiro et al., 2011), while low-pressure and high fault-stress locations are more probable to host runaway ruptures (e.g., Galis et al., 2017; Gischig, 2015). One distinct earthquake behavior related to the governing force is the rupture direction with respect to the injection wells, where rupture toward the well is more probable in pore-pressure driven environments with high injection pressures (Dempsey & Suckale, 2016). In observational studies, this has been observed particularly in the largest events at both deep geothermal and high-rate wastewater injection sites ($M_L > 1.8$, Folesky et al., 2016; M_w 5.1–5.7, Lui & Huang, 2019; M_w 3.3, Kiraly-Proad et al., 2019). The induced seismicity from the Helsinki geothermal stimulation is primarily pore-pressure driven, as evidenced by $M_{\max}$ being relatively low and following the Galis et al. (2017) model for stable, pressure-controlled injection and the seismicity mainly constrained to the diffusion cloud (Kwiatek et al., 2019). However, we do not observe a directivity bias for rupture toward the well amongst the largest Helsinki events. Indeed, only one event ruptures toward the well (event 4364, M_L 1.7, see Figure 6), although when the proximity to the well (55 m) and the catalog location uncertainty (52 m; Leonhardt, Kwiatek, Martínez-Garzón, Bohnhoff, et al., 2021) are considered, the rupture angle becomes less stable (see Figure S39 in Supporting Information S1). If we also consider the two events with two possible rupture directions, one of the events (6246, M_L 1.5) has a plane with a preferred rupture toward the well that is more stable. Thus, at best, this results in two out of 12 events which appear to rupture back toward the well. Dempsey and Suckale (2016) examined directivity bias as a distribution of directivity observations from different pressure evolution scenarios, also determining the smallest number of samples required to establish directivity bias at a site using Kolmogorov-Smirnov testing. They found that for the scenario applicable to EGS sites

("advancing-front" scenario where permeability enhancement dominates), the directivity bias was so strong that only five observations were required to detect it (see Figure 14 in Dempsey & Suckale, 2016). Thus, the Helsinki site appears to not exhibit the expected rupture direction behavior, especially considering that the same number of events rupture away from the well (events 6389 and 5695) as toward. Instead, the preferred rupture direction seems to be roughly parallel to the well, displayed by eight out of the 12 events.

One common assumption in rupture growth models is that earthquake nucleation initiates at the pore pressure front (e.g., Dempsey & Suckale, 2016; McClure & Horne, 2011), which has a steeper gradient at the beginning of stimulation. Meanwhile, the studied Helsinki events occur at the earliest during stage 2, most occur during stages 4–5, and they locate toward the bottom of the seismicity cluster (Figure 6). Thus, this suggests these events occurred in a highly stressed rock volume continuously supplied with new fluids. In the absence of a distinct pore pressure front, it is possible that the pressure gradient no longer controlled the directivity of the largest events to the same extent as during early stimulation stages. Instead, later events could be expressing the local stress heterogeneities, stress concentrations, and structure of the fracture zone, allowing for alternative rupture directions. Unfortunately, only one event (event 1585) from stimulation stage 1 was large enough to be included in this study and it did not display any clear directivity, preventing us from examining any possible rupture directivity bias during the early stages when the pore pressure gradient was steeper. For the later stages, the Helsinki earthquakes show a preference toward parallel directivity with respect to the well, possibly indicating that the local fracture zone is controlling the rupture process. Interestingly, this is the opposite behavior to what Folesky et al. (2016) observed with their smaller events. While their largest events ($M_L \geq 1.8$) ruptured back toward the well, the smaller events displayed an increasingly clearer trend of orientation with distance away from the open hole. They suggested that the increased pore pressure controls the rupture process in the vicinity of the borehole (<100 m), resulting in no clear trend in rupture directions, and that either the stress field or geological structure takes over once the pore pressure influence decreases. For the Helsinki events, seven out of the nine events within 100 m (and the increased pore pressure cloud) display parallel directivity to the well (see Figure 6c).

Rupture growth models also typically consider a single, isolated fault or fracture that allows for clear stress concentration and transfer (e.g., Dempsey & Suckale, 2016; McClure & Horne, 2011), rather than a fracture network in which fluid can take more complex paths, especially toward the end of stimulation. Indeed, in Helsinki, the refined focal mechanisms obtained using the PCA approach indicate reactivation of a network of parallel fractures, supporting earlier interpretations (Hillers et al., 2020; Kwiatek et al., 2019; Leonhardt, Kwiatek, Martínez-Garzón, Bohnhoff, et al., 2021). Hydraulically stimulated fractures are generally a combination of hydrofracking (mode I, tensile opening) and hydroshearing (mode II and III, in-plane and out-of-plane shearing, respectively) (e.g., Frash et al., 2019). Reactivation of a pre-existing fracture network, which is a likely mechanism of the seismicity during the 2018 Helsinki simulation (cf. discussion in Kwiatek et al., 2019; Leonhardt, Kwiatek, Martínez-Garzón, Bohnhoff, et al., 2021), tends to predominantly result in hydroshearing as it allows for slip at lower pressures than hydrofracking (e.g., Pogacnik et al., 2016). This is supported by the small non-double couple components observed in our moment tensor solutions. Moreover, we find that the Helsinki microseismic events are predominantly mode II failures rather than mode III (Figure 7). Generally, strike-slip faults are initially modeled as mode III and thrust/normal faults as mode II (e.g., Gudmundsson, 2014; Oglesby et al., 2000). Thus, a preference toward mode II failures agrees with the oblique reverse faulting source mechanisms observed at the Helsinki site. In contrast, Dempsey and Suckale (2016) modeled strike-slip faults in their numerical analysis, assuming mode III failures. We also investigate if we would be able to detect a mode III rupture given the dominant focal mechanism and station configuration in Helsinki by modeling the expected directivity patterns from both pure mode II and mode III failures and retrieving the range in θ_i found for each mode (see Figure S40 in Supporting Information S1). We find that for mode II ruptures we will have a θ_i coverage of 78°, while mode III produces a coverage of 55°, thus it easier to detect mode II failures. However, the event closest to a mode III failure (event 7641, see Figure 7) also had the smallest change in observed f_{ci} over its stations (22–37 Hz) with a low resolved rupture velocity ($v_r = 0.20\beta$, see Table S2 in Supporting Information S1) and was still resolvable in terms of directivity and rupture direction (see Figure S31 in Supporting Information S1). Radiation pattern is another factor that could affect the resolvability of mode III failures. Any stations located in the direction of the B-axis (or null-axis) would observe damped amplitudes due to unfavorable radiation pattern of the S-wave and could potentially bias the directivity pattern. However, because the Helsinki events do not have any station coverage over the B-axis, we do not consider this to significantly affect our results. Investigating the implications of a mode II preference over mode III is outside of the scope of this article, instead these results can

be used by geomechanical modelers as observations to better understand fracture mechanics of fluid injected into fracture zones.

Finally, in the directivity inversion, we generally obtain low (~0.19–0.66β) rupture velocities (see Table S2 in Supporting Information S1). Low v_r may indicate that more elastic strain energy is spent on fracture reactivation rather than radiation of seismic waves (e.g., Kanamori & Rivera, 2004; Kwiatek et al., 2011; Prieto et al., 2017), which seems feasible in a complex distributed fracture network. However, v_r can be difficult to constrain in directivity analyses. For example, Abercrombie, Poli, and Bannister (2017) found that resolution and frequency limitations significantly affect v_r. While we synthetically investigated the minimum resolution for a symmetrical pulse (see Figures S34–S38 in Supporting Information S1), the ASTF pulses could vary in shape and might in some cases be under- or overestimated. v_r is also sensitive to the assumed $\tau \propto 1/f_c$ relationship. If we use $\tau_i = 1/f_{ci}$ instead of Equation 5, the rupture directions of the nodal planes stay the same but the obtained v_r range increases to 0.37–0.90 β, which results in the median v_r increasing from 0.40 β using Equation 5 to 0.63 β. While we deemed $\tau = 1/f_c$ not appropriate for the Helsinki earthquakes due to overestimation at longer τ and lower f_c (see Figure 4), our ASTFs pulses were measured at 0.1 times the maximum amplitude due to the noise levels on either side of the pulse. For a symmetrical pulse, this results in a 5% smaller width (see Figures S34–S38 in Equation 5). However, considering the τ_i uncertainties were set to ±0.002 s (i.e., the sampling step) and a 5% mismatch for the widest observed pulse (0.033 s) would lead to 0.0016 s error, it falls within the τ_i uncertainty. Finally, non-unilateral ruptures may lead to underestimated rupture velocities (Tomic et al., 2009). While we observe complex station ASTFs for eight of the events, indicating an additional rupture of a possible subevent or asperity that could lead to biased f_{ci} estimates, we did not identify clear bilateral ruptures.

7. Conclusion

We investigated the rupture behavior of fluid-induced microseismicity from the 2018 St1 Deep Heat geothermal hydraulic stimulation campaign in Helsinki using directivity and focal mechanisms, resolving rupture directions for nine of the largest events in a pore-pressure driven environment. We find rupture directions are variable with respect to the injection well, with one event rupturing toward, two rupturing away (including the largest event , M_L 1.9), and the remaining rupturing roughly parallel to the well. This is contrary to predictions by rupture growth models, which commonly assume a strong pressure gradient exists. These events occurred toward the end of stimulation and near the well, indicating that rupture directions may be more random when the pore-pressure gradient is weaker due to prolonged injection. Finally, we find that the events exhibit a preference toward mode II failure (parallel slip and rupture directions). These observations provide new constraints for mechanical models of rupture growth in pore-pressure dominated settings.

Data Availability Statement

All waveform data used is available in the associated data publication (Holmgren et al., 2022). Full earthquake catalog can be obtained through Leonhardt, Kwiatek, Martínez-Garzón, and Heikkinen (2021).

Acknowledgments
We thank St1 Deep Heat Oy for providing the data. We thank the editor Rachel Abercrombie, the associate editor, David Dempsey, German Prieto, Jonas Folesky, and one anonymous reviewer for valuable comments which have improved this work. We also thank Germán Rodríguez, James Verdon, Ulrich Wegler, Tom Eulenfeld, and Adam Klinger for helpful discussions. This work was funded by the Natural Environment Research Council (NERC) (NE/R017956/1, "EQUIPT4RISK").

References

Abercrombie, R. E. (1995). Earthquake source scaling relationships from− 1 to 5 ML using seismograms recorded at 2.5-km depth. *Journal of Geophysical Research*, *100*(B12), 24015–24036. https://doi.org/10.1029/95JB02397

Abercrombie, R. E., Bannister, S., Ristau, J., & Doser, D. (2017). Variability of earthquake stress drop in a subduction setting, the Hikurangi Margin, New Zealand. *Geophysical Journal International*, *208*(1), 306–320. https://doi.org/10.1093/gji/ggw393

Abercrombie, R. E., Poli, P., & Bannister, S. (2017). Earthquake directivity, orientation, and stress drop within the subducting plate at the Hikurangi margin, New Zealand. *Journal of Geophysical Research: Solid Earth*, *122*(12), 10176–10188. https://doi.org/10.1002/2017JB014935

Archuleta, R. J., & Ji, C. (2016). Moment rate scaling for earthquakes 3.3≤ M≤ 5.3 with implications for stress drop. *Geophysical Research Letters*, *43*(23), 12004–12011. https://doi.org/10.1002/2016GL071433

Bakun, W. H., & Bufe, C. G. (1975). Shear-wave attenuation along the San Andreas Fault zone in central California. *Bulletin of the Seismological Society of America*, *65*(2), 439–459. https://doi.org/10.1785/BSSA0650020439

Bentz, S., Martínez-Garzón, P., Kwiatek, G., Bohnhoff, M., & Renner, J. (2018). Sensitivity of full moment tensors to data preprocessing and inversion parameters: A case study from the Salton Sea geothermal field. *Bulletin of the Seismological Society of America*, *108*(2), 588–603. https://doi.org/10.1785/0120170203

Boatwright, J. (1980). A spectral theory for circular seismic sources; simple estimates of source dimension, dynamic stress drop, and radiated seismic energy. *Bulletin of the Seismological Society of America*, *70*(1), 1–27. https://doi.org/10.1785/BSSA0700010001

Brune, J. N. (1970). Tectonic stress and the spectra of seismic shear waves from earthquakes. *Journal of Geophysical Research*, *75*(26), 4997–5009. https://doi.org/10.1029/JB075i026p04997

Catalli, F., Rinaldi, A. P., Gischig, V., Nespoli, M., & Wiemer, S. (2016). The importance of earthquake interactions for injection-induced seismicity: Retrospective modeling of the Basel Enhanced Geothermal System. *Geophysical Research Letters*, *43*(10), 4992–4999. https://doi.org/10.1002/2016GL068932

Courboulex, F., Vallée, M., Causse, M., & Chounet, A. (2016). Stress-drop variability of shallow earthquakes extracted from a global database of source time functions. *Seismological Research Letters*, *87*(4), 912–918. https://doi.org/10.1785/0220150283

Dempsey, D., & Suckale, J. (2016). Collective properties of injection-induced earthquake sequences: 1. Model description and directivity bias. *Journal of Geophysical Research: Solid Earth*, *121*(5), 3609–3637. https://doi.org/10.1002/2015JB012550

Denolle, M. A., & Shearer, P. M. (2016). New perspectives on self-similarity for shallow thrust earthquakes. *Journal of Geophysical Research: Solid Earth*, *121*(9), 6533–6565. https://doi.org/10.1002/2016JB013105

Diehl, T., Kraft, T., Kissling, E., & Wiemer, S. (2017). The induced earthquake sequence related to the St. Gallen deep geothermal project (Switzerland): Fault reactivation and fluid interactions imaged by microseismicity. *Journal of Geophysical Research: Solid Earth*, *122*(9), 7272–7290. https://doi.org/10.1002/2017JB014473

Domański, B., & Gibowicz, S. J. (2008). Comparison of source parameters estimated in the frequency and time domains for seismic events at the Rudna copper mine, Poland. *Acta Geophysica*, *56*(2), 324–343. https://doi.org/10.2478/s11600-008-0014-1

Domański, B., Gibowicz, S. J., & Wiejacz, P. (2002). Source time function of seismic events at Rudna copper mine, Poland. In *The mechanism of induced seismicity* (pp. 131–144). https://doi.org/10.1007/978-3-0348-8179-1_6

Eulenfeld, T., Hillers, G., Vuorinen, T. A. T., & Wegler, U. (2022). Induced earthquake source parameters, attenuation, and site effects from waveform envelopes in the Fennoscandian Shield. arXiv, arXiv:2207.05545, 12 July 2022. https://doi.org/10.48550/arXiv.2207.05545

Fan, W., & McGuire, J. J. (2018). Investigating microearthquake finite source attributes with IRIS community wavefield demonstration experiment in Oklahoma. *Geophysical Journal International*, *214*(2), 1072–1087. https://doi.org/10.1093/gji/ggy203

Fletcher, J. B., & Boatwright, J. (2020). Directivity of M 3.1 earthquake near Anza, California and the effect on peak ground motion. *Bulletin of the Seismological Society of America*, *110*(1), 312–318. https://doi.org/10.1785/0120190141

Folesky, J., Kummerow, J., Shapiro, S. A., Häring, M., & Asanuma, H. (2016). Rupture directivity of fluid-induced microseismic events: Observations from an enhanced geothermal system. *Journal of Geophysical Research: Solid Earth*, *121*(11), 8034–8047. https://doi.org/10.1002/2016JB013078

Frankel, A., Fletcher, J., Vernon, F., Haar, L., Berger, J., Hanks, T., & Brune, J. (1986). Rupture characteristics and tomographic source imaging of ML∼ 3 earthquakes near Anza, southern California. *Journal of Geophysical Research*, *91*(B12), 12633–12650. https://doi.org/10.1029/JB091iB12p12633

Frash, L. P., Hampton, J., Gutierrez, M., Tutuncu, A., Carey, J. W., Hood, J., et al. (2019). Patterns in complex hydraulic fractures observed by true-triaxial experiments and implications for proppant placement and stimulated reservoir volumes. *Journal of Petroleum Exploration and Production Technology*, *9*(4), 2781–2792. https://doi.org/10.1007/s13202-019-0681-2

Galis, M., Ampuero, J. P., Mai, P. M., & Cappa, F. (2017). Induced seismicity provides insight into why earthquake ruptures stop. *Science Advances*, *3*(12), eaap7528. https://doi.org/10.1126/sciadv.aap7528

Gischig, V. S. (2015). Rupture propagation behavior and the largest possible earthquake induced by fluid injection into deep reservoirs. *Geophysical Research Letters*, *42*(18), 7420–7428. https://doi.org/10.1002/2015GL065072

Gudmundsson, A. (2014). Elastic energy release in great earthquakes and eruptions. *Frontiers of Earth Science*, *2*, 10. https://doi.org/10.3389/feart.2014.00010

Hartzell, S. H. (1978). Earthquake aftershocks as Green's functions. *Geophysical Research Letters*, *5*(1), 1–4. https://doi.org/10.1029/GL005i001p00001

Haskell, N. A. (1964). Total energy and energy spectral density of elastic wave radiation from propagating faults. *Bulletin of the Seismological Society of America*, *54*(6A), 1811–1841. https://doi.org/10.1785/BSSA05406A1811

Hillers, G., T. Vuorinen, T. A., Uski, M. R., Kortström, J. T., Mäntyniemi, P. B., Tiira, T., et al. (2020). The 2018 geothermal reservoir stimulation in Espoo/Helsinki, Southern Finland: Seismic network anatomy and data features. *Seismological Research Letters*, *91*(2A), 770–786. https://doi.org/10.1785/0220190253

Hisada, Y. (2000). A theoretical omega-square model considering the spatial variation in slip and rupture velocity. *Bulletin of the Seismological Society of America*, *90*(2), 387–400. https://doi.org/10.1785/0119990083

Holmgren, J. M., Atkinson, G. M., & Ghofrani, H. (2019). Stress drops and directivity of induced earthquakes in the Western Canada Sedimentary Basin. *Bulletin of the Seismological Society of America*, *109*(5), 1635–1652. https://doi.org/10.1785/0120190035

Holmgren, J. M., Kwiatek, G., & Werner, M. J. (2022). Seismic waveforms of fluid-induced seismicity from the 2018 hydraulic stimulation campaign at the OTN-3 well, Helsinki, Finland. V. 1.0. *GFZ Data Services*. https://doi.org/10.5880/fidgeo.2022.012

Huang, Y., Ellsworth, W. L., & Beroza, G. C. (2017). Stress drops of induced and tectonic earthquakes in the central United States are indistinguishable. *Science Advances*, *3*(8), e1700772. https://doi.org/10.1126/sciadv.1700772

Ide, S., Beroza, G. C., Prejean, S. G., & Ellsworth, W. L. (2003). Apparent break in earthquake scaling due to path and site effects on deep borehole recordings. *Journal of Geophysical Research*, *108*(B5), 2271. https://doi.org/10.1029/2001JB001617

Igonin, N., Verdon, J. P., Kendall, J. M., & Eaton, D. W. (2021). Large-scale fracture systems are permeable pathways for fault activation during hydraulic fracturing. *Journal of Geophysical Research: Solid Earth*, *126*(3), e2020JB020311. https://doi.org/10.1029/2020JB020311

Jost, M. L., Büßelberg, T., Jost, Ö., & Harjes, H. P. (1998). Source parameters of injection-induced microearthquakes at 9 km depth at the KTB deep drilling site, Germany. *Bulletin of the Seismological Society of America*, *88*(3), 815–832. https://doi.org/10.1785/BSSA0880030815

Kakkuri, J., & Chen, R. (1992). On horizontal crustal strain in Finland. *Bulletin Geodesique*, *66*(1), 12–20. https://doi.org/10.1007/BF00806806

Kanamori, H., & Rivera, L. (2004). Static and dynamic scaling relations for earthquakes and their implications for rupture speed and stress drop. *Bulletin of the Seismological Society of America*, *94*(1), 314–319. https://doi.org/10.1785/0120030159

Kettlety, T., Verdon, J. P., Werner, M. J., Kendall, J. M., & Budge, J. (2019). Investigating the role of elastostatic stress transfer during hydraulic fracturing-induced fault activation. *Geophysical Journal International*, *217*(2), 1200–1216. https://doi.org/10.1093/gji/ggz080

Király-Proag, E., Satriano, C., Bernard, P., & Wiemer, S. (2019). Rupture process of the Mw 3.3 earthquake in the St. Gallen 2013 geothermal reservoir, Switzerland. *Geophysical Research Letters*, *46*(14), 7990–7999. https://doi.org/10.1029/2019GL082911

Kwiatek, G. (2008). Relative source time functions of seismic events at the Rudna copper mine, Poland: Estimation of inversion uncertainties. *Journal of Seismology*, *12*(4), 499–517. https://doi.org/10.1007/s10950-008-9100-8

Kwiatek, G., & Ben-Zion, Y. (2020). Detection limits and near-field ground motions of fast and slow earthquakes. *Journal of Geophysical Research: Solid Earth*, *125*(7), e2019JB018935. https://doi.org/10.1029/2019JB018935

Kwiatek, G., Martínez-Garzón, P., & Bohnhoff, M. (2016). HybridMT: A MATLAB/shell environment package for seismic moment tensor inversion and refinement. *Seismological Research Letters*, *87*(4), 964–976. https://doi.org/10.1785/0220150251

Kwiatek, G., Plenkers, K., & Dresen, G., & JAGUARS Research Group. (2011). Source parameters of picoseismicity recorded at Mponeng deep gold mine, South Africa: Implications for scaling relations. *Bulletin of the Seismological Society of America*, *101*(6), 2592–2608. https://doi.org/10.1785/0120110094

Kwiatek, G., Saarno, T., Ader, T., Bluemle, F., Bohnhoff, M., Chendorain, M., et al. (2019). Controlling fluid-induced seismicity during a 6.1-km-deep geothermal stimulation in Finland. *Science Advances*, *5*(5), eaav7224. https://doi.org/10.1126/sciadv.aav7224

Lanza, V., Spallarossa, D., Cattaneo, M., Bindi, D., & Augliera, P. (1999). Source parameters of small events using constrained deconvolution with empirical Green's functions. *Geophysical Journal International*, *137*(3), 651–662. https://doi.org/10.1046/j.1365-246x.1999.00809.x

Leonhardt, M., Kwiatek, G., Martínez-Garzón, P., Bohnhoff, M., Saarno, T., Heikkinen, P., & Dresen, G. (2021). Seismicity during and after stimulation of a 6.1 km deep enhanced geothermal system in Helsinki, Finland. *Solid Earth*, *12*(3), 581–594. https://doi.org/10.5194/se-12-581-2021

Leonhardt, M., Kwiatek, G., Martínez-Garzón, P., & Heikkinen, P. (2021). Earthquake catalog of induced seismicity recorded during and after stimulation of Enhanced Geothermal System in Helsinki, Finland. *GFZ Data Services*. https://doi.org/10.5880/GFZ.4.2.2021.001

Li, Y., Doll, C., Jr., & Toksöz, M. N. (1995). Source characterization and fault plane determination for MbLg = 1.2 to 4.4 earthquakes in the Charlevoix seismic zone, Quebec, Canada. *Bulletin of the Seismological Society of America*, *85*(6), 1604–1621. https://doi.org/10.1785/BSSA0850061604

Lui, S. K., & Huang, Y. (2019). Do injection-induced earthquakes rupture away from injection wells due to fluid pressure change? *Bulletin of the Seismological Society of America*, *109*(1), 358–371. https://doi.org/10.1785/0120180233

McClure, M. W., & Horne, R. N. (2011). Investigation of injection-induced seismicity using a coupled fluid flow and rate/state friction model. *Geophysics*, *76*(6), WC181–WC198. https://doi.org/10.1190/geo2011-0064.1

Meng, Q., Ni, S., & Peng, Z. (2021). Complex source behaviors and spatio-temporal evolution of seismicity during the 2015-2016 earthquake sequence in Cushing, Oklahoma. *Journal of Geophysical Research: Solid Earth*, *126*(6), e2021JB022168. https://doi.org/10.1029/2021JB022168

Mori, J., & Frankel, A. (1990). Source parameters for small events associated with the 1986 North Palm Springs, California, earthquake determined using empirical Green functions. *Bulletin of the Seismological Society of America*, *80*(2), 278–295. https://doi.org/10.1785/BSSA0800020278

Mueller, C. S. (1985). Source pulse enhancement by deconvolution of an empirical Green's function. *Geophysical Research Letters*, *12*(1), 33–36. https://doi.org/10.1029/GL012i001p00033

Oglesby, D. D., Archuleta, R. J., & Nielsen, S. B. (2000). The three-dimensional dynamics of dipping faults. *Bulletin of the Seismological Society of America*, *90*(3), 616–628. https://doi.org/10.1785/0119990113

Onwuemeka, J., Liu, Y., & Harrington, R. M. (2018). Earthquake stress drop in the Charlevoix seismic zone, eastern Canada. *Geophysical Research Letters*, *45*(22), 12226–12235. https://doi.org/10.1029/2018GL079382

Park, S., & Ishii, M. (2015). Inversion for rupture properties based upon 3-D directivity effect and application to deep earthquakes in the Sea of Okhotsk region. *Geophysical Journal International*, *203*(2), 1011–1025. https://doi.org/10.1093/gji/ggv352

Pogacnik, J., Elsworth, D., O'Sullivan, M., & O'Sullivan, J. (2016). A damage mechanics approach to the simulation of hydraulic fracturing/shearing around a geothermal injection well. *Computers and Geotechnics*, *71*, 338–351. https://doi.org/10.1016/j.compgeo.2015.10.003

Prieto, G. A., Froment, B., Yu, C., Poli, P., & Abercrombie, R. (2017). Earthquake rupture below the brittle-ductile transition in continental lithospheric mantle. *Science Advances*, *3*(3), e1602642. https://doi.org/10.1126/sciadv.1602642

Prieto, G. A., Parker, R. L., & Vernon, F. L., III. (2009). A Fortran 90 library for multitaper spectrum analysis. *Computers & Geosciences*, *35*(8), 1701–1710. https://doi.org/10.1016/j.cageo.2008.06.007

Seo, M. S., Kim, W. Y., & Kim, Y. (2022). Rupture directivity of the 2021 ML 2.2 Gwangyang, Korea, microearthquake: Toward resolving high-resolution rupture process of a small earthquake. *The Seismic Record*, *2*(4), 227–236. https://doi.org/10.1785/0320220030

Shapiro, S. A., Krüger, O. S., Dinske, C., & Langenbruch, C. (2011). Magnitudes of induced earthquakes and geometric scales of fluid-stimulated rock volumes. *Geophysics*, *76*(6), WC55–WC63. https://doi.org/10.1190/geo2010-0349.1

Spudich, P., & Chiou, B. S. (2008). Directivity in NGA earthquake ground motions: Analysis using isochrone theory. *Earthquake Spectra*, *24*(1), 279–298. https://doi.org/10.1193/1.2928225

Tomic, J., Abercrombie, R. E., & Do Nascimento, A. F. (2009). Source parameters and rupture velocity of small M ≤ 2.1 reservoir induced earthquakes. *Geophysical Journal International*, *179*(2), 1013–1023. https://doi.org/10.1111/j.1365-246X.2009.04233.x

Uchide, T., & Imanishi, K. (2016). Small earthquakes deviate from the omega-square model as revealed by multiple spectral ratio analysis. *Bulletin of the Seismological Society of America*, *106*(3), 1357–1363. https://doi.org/10.1785/0120150322

Van Houtte, C., & Denolle, M. (2018). Improved model fitting for the empirical Green's function approach using hierarchical models. *Journal of Geophysical Research: Solid Earth*, *123*(4), 2923–2942. https://doi.org/10.1002/2017JB014943

Vavrycuk, V., Adamova, P., Doubravová, J., & Jakoubková, H. (2017). Moment tensor inversion based on the principal component analysis of waveforms: Method and application to microearthquakes in west Bohemia, Czech Republic. *Seismological Research Letters*, *88*(5), 1303–1315. https://doi.org/10.1785/0220170027

Viegas, G., Abercrombie, R. E., & Kim, W. Y. (2010). The 2002 M5 Au Sable Forks, NY, earthquake sequence: Source scaling relationships and energy budget. *Journal of Geophysical Research*, *115*(B7), B07310. https://doi.org/10.1029/2009JB006799